Research article

Jing Wang, Dong Liang, Zehua Qu, Ivan M. Kislyakov, Valery M. Kiselev and Jun Liu*

PEGylated-folic acid–modified black phosphorus quantum dots as near-infrared agents for dual-modality imaging-guided selective cancer cell destruction

https://doi.org/10.1515/nanoph-2019-0506
Received December 7, 2019; revised January 12, 2020; accepted January 13, 2020

Abstract: Biological systems have high transparence to 700–1100-nm near-infrared (NIR) light. Black phosphorus quantum dots (BPQDs) have high optical absorbance in this spectrum. This optical property of BPQDs integrates both diagnostic and therapeutic functions together in an all-in-one processing system in cancer theranostic approaches. In the present study, BPQDs were synthesized and functionalized by targeting moieties (PEG-NH_2-FA) and were further loaded with anticancer drugs (doxorubicin) for photodynamic–photothermal–chemotherapy. The precise killing of cancer cells was achieved by linking BPQDs with folate moiety (folic acid), internalizing BPQDs inside cancer cells with folate receptors and NIR triggering, without affecting the receptor-free cells. These *in vitro* experiments confirm that the agent exhibited an efficient photokilling effect and a light-triggered and heat-induced drug delivery at the precise tumor sites. Furthermore, the nanoplatform has good biocompatibility and effectively obliterates tumors in nude mice, showing no noticeable damages to noncancer tissues. Importantly, this nanoplatform can inhibit tumor growth through visualized synergistic treatment and photoacoustic and photothermal imaging. The present design of versatile nanoplatforms can allow for the adjustment of nanoplatforms for good treatment efficacy and multiplexed imaging, providing an innovation for targeted tumor treatment.

Keywords: black phosphorus quantum dots; targeted; synergistic therapy; photoacoustic imaging; drug release.

1 Introduction

Cancer remains as a major disease with high morbidity and mortality [1, 2]. Radiation, chemotherapy, surgery, and combined strategies remain as the cornerstone in cancer treatment [3, 4]. However, these treatment methods often have poor efficacy due to the lack of targeting abilities and severe side effects [5, 6]. Nanosystems have been proposed with minimal invasiveness and high effectiveness, integrating diagnosis and drug delivery [6]. Theranostic nanoplatforms with photodynamic therapy (PDT), photothermal therapy (PTT), chemotherapy, and multimodal imaging are expected to achieve better treatment efficacy, when compared to monotherapies [7, 8].

The newly discovered black phosphorus quantum dots (BPQDs) present an intriguing advantage in the field of biomedicine [9–11]. A BPQD is a metal-free layered semiconductor and has a thickness-dependent band gap that can be tuned from 0.3 eV for bulk to 2.0 eV for single layer [12]. Black phosphorus (BP) has a higher ratio of surface to volume, when compared to other two-dimensional (2D) materials [13–15], such as selenium, transition metal disulfide (TMD), and graphene, for the puckered lattice configuration. This property of BP may increase its capacity for drug loading. Black phosphorus is also a highly efficient photosensitizer for unique electronic structures and has been used to generate singlet oxygen for PDT [16]. The nanoparticles (NPs) and quantum dots of BP both have a wide absorption of visible light spectrum, possessing the near-infrared (NIR) photothermal properties for PTT [17].

***Corresponding author: Jun Liu,** State Key Laboratory of High Field Laser Physics, Shanghai Institute of Optics and Fine Mechanics, Chinese Academy of Sciences, Shanghai 201800, China; and Center of Materials Science and Optoelectronics Engineering, University of Chinese Academy of Sciences, Beijing 100049, China, e-mail: jliu@siom.ac.cn
Jing Wang and Dong Liang: State Key Laboratory of High Field Laser Physics, Shanghai Institute of Optics and Fine Mechanics, Chinese Academy of Sciences, Shanghai 201800, China. https://orcid.org/0000-0003-3684-1015 (J. Wang)
Zehua Qu: State Key Laboratory of Molecular Engineering of Polymers, Department of Macromolecular Science, Fudan University, 2205 Songhu Road, Shanghai 200433, China
Ivan M. Kislyakov: State Key Laboratory of High Field Laser Physics, Shanghai Institute of Optics and Fine Mechanics, Chinese Academy of Sciences, Shanghai 201800, China; and S. I. Vavilov State Optical Institute, 5/2 Kadetskaya Line, Saint Petersburg 199053, Russia
Valery M. Kiselev: S. I. Vavilov State Optical Institute, 5/2 Kadetskaya Line, Saint Petersburg 199053, Russia

Thus, BPQDs can reduce economic problems and ecological concerns and degrade in aqueous medium, forming nontoxic phosphate and phosphonate. Furthermore, phosphorus, which makes up approximately 1% of total body weight in humans, is an essential element that is inherently biocompatible [18]. Therefore, BP is considered suitable for developing novel delivery systems for cancer treatment.

Folate receptor (FR) is expressed in many cancer cells and can be targeted by folic acid (FA) for delivering drugs [19, 20] to HeLa cells [21], 293T cells [22], and ovarian tumors [23]. The present study aimed to investigate the anticancer effect of a drug delivery system that targets FR in a mouse tumor model of 293T cells.

2 Experimental section

2.1 Concept of the drug delivery system

The drug delivery system was named FA-PEG@BPQD@DOX (Figure 1). Briefly, the nanocomposites are administered. Then, a laser was used to induce the production of reactive oxygen and heat in the BPQD, resulting in cell damage. In the meantime, the temperature was raised, and the drug was released from the nanocomposite. The cell lethality of FA-PEG@BPQD@DOX was approximately 10 times of PEG@BPQD@DOX with the same irradiation, which could mean biological and clinical significance.

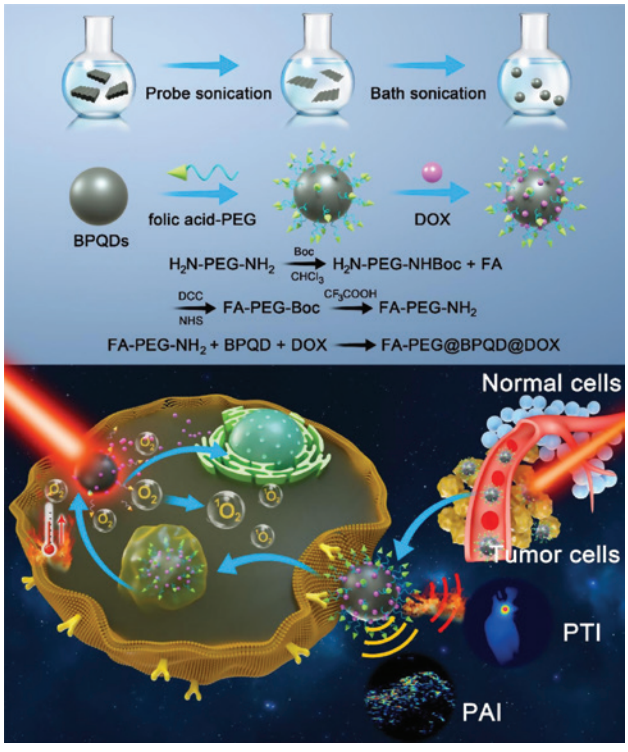

Figure 1: A schematic of the preparation of the FA-PEG@BPQD@DOX nanocomposite and its anticancer mechanism of the combination of photodynamic therapy, photothermal therapy, and chemotherapy.

2.2 Materials

Bulk BP crystals were obtained from XFNANO Materials Tech (Nanjing, China) and kept in a dark glovebox filled with Ar. The FA, polyethylene glycol (PEG, Mw = 5000), N-(3-dimethylaminopropyl)-N′-ethylcarbodiimide hydrochloride (99%), and N-hydroxysuccinimide (NHS, 98%) were purchased from J&K Chemical, Ltd. The doxorubicin hydrochloride (DOX) was purchased from Beijing Maiso Chemical Technology. Dulbecco modified Eagle medium (DMEM), fetal bovine serum, penicillin (100 mg/ml), streptomycin (100 mg/ml), phosphate-buffered saline (PBS), and 3-(4,5-dimethylthiazol-2-yl)-2,5-diphenyl-tetrazolium bromide (MTT) were obtained from Invitrogen (Carlsbad, CA, USA). All experiments used deionized water (Milli-Q System; Millipore, MA, USA).

2.3 Characterization

The morphology and structure of the obtained nanocomposite were examined using a transmission electron microscope (TEM; JEM-2100HR; JEOL, Japan) operating at 120 kV and an atomic force microscope (AFM; FM-Nanoview 1000; FSM-Precision, China). Raman scattering was excited using a 633-nm laser (Horiba Jobin-Yvon Lab Ram HR VIS). The spectra of the absorption were recorded using a Perkin–Elmer UV-vis-NIR Lambda 750 spectrometer. The dynamic light scattering (DLS) and zeta potential were measured at 25°C (Zetasizer Nano ZS90 analyzer; Malvern Instruments, UK). Confocal laser scanning microscopy was performed using a laser scanning confocal microscope (Nikon, Japan). The photothermal effects were evaluated using an 808-nm consecutive NIR laser with a spot size of 5 × 5 mm (Changchun New Industries Optoelectronics Technology, China). The thermal images were obtained using an infrared thermal-imaging camera, with an accuracy of 0.1°C (InfraTec; VarioCAM™ Research, Germany). Both photoacoustic (PA) and ultrasound (US) images were taken with a consecutive excitation of 680–970 nm and a focal depth of 2 cm (VevoLAZR; FujiFilm VisualSonics, Mountain View, CA, USA).

2.4 Preparation of BPQDs

The BPQDs were synthesized according to a previous report [24]. First, the bulk BP was triturated into BP powder using a mortar. Then, approximately 40 mg of BP powder and 20 mg of NaOH were gently mixed with 30 ml of n-methylpyrrolidone. This mixture was mildly stirred for 8 h at 150°C. Then, the bulk BP was removed by centrifugation (3000 rpm, 10 min). Afterward, the BPQD products were further centrifuged at 30,000 rpm for 20 min, repeatedly washed with water, and dispersed in deionized water.

2.5 The synthesis of FA-PEG@BPQD@DOX

Folic acid was linked to PEG-diamine (H_2N-PEG-NH_2), forming FA-PEG-NH_2 [25]. Briefly, 0.5 g of BoC_2O was dissolved in 10 ml of chloroform ($CHCl_3$) and cooled to 0°C. Then, the solution was added dropwise to 25 ml of anhydrous $CHCl_3$ containing 5 g of PEG. The reaction lasted for 24 h at room temperature. Next, a gummy oil was obtained and added into 50 ml of CH_2Cl_2, which was washed in 200 ml of NaCl solution for several times and dried with the help of Na_2SO_4. After running over filter paper, the solvent was removed in reduced pressure. Then, FA (0.5 g) was dissolved in 20 ml of dimethyl sulfoxide, was added with DCC and NHS, and was stirred in the dark for 24 h. Afterward, the reaction byproducts were removed by filtration using polyvinylidene fluoride membrane. The FA-NHS was precipitated using ethanol and ether and washed using ether. Dimethyl sulfoxide (20 ml) was added with 0.3 g of FA-NHS and 0.4 g of PEG-Boc and was stirred overnight. A yellow precipitation was formed by the addition of ethanol and ether and was washed in ether. Then, this was added with 5 ml of trifluoroacetic acid (TFA) and stirred for 5 h. Under reduced pressure, the TFA was eliminated, during which 15 ml of dimethylformamide was added. The precipitation was washed, as previously described. The excessive FA was removed, and the final PEG-Boc was lyophilized and stored.

Black phosphorus quantum dots of 1 mg were dispersed in 5 ml of water and mixed with 5 mg of FA-PEG-NH_2. Then, the mixture was sonicated for 1 h and stirred for 6 h. Afterward, the excess FA-PEG-NH_2 was removed by centrifugation at 10,000 rpm and washed with water, resulting in FA-PEG@BPQD. The PEG-BPQDs were prepared using the same method.

For DOX loading, an FA-PEG@BPQD solution was added with DOX and vigorously stirred at room temperature for 24 h. The, the supernatant was removed by centrifugation. The resulting FA-PEG@BPQD@DOX nanocomposites were resuspended in PBS. The DOX concentration in the supernatant was measured using ultraviolet-visible (UV-vis) spectral analysis and a standard curve. The amount of nanoparticle-loaded DOX was calculated by subtracting the measured amount of DOX from that added at the beginning.

2.6 Detection of $^1O_2$

The characterization of reactive oxygen species (ROS) was performed using the photo-oxidation of 1,3-diphenylisobenzofuran (DPBF). The ROS rapidly oxidized DPBF to *o*-dibenzoylbenzene, resulting in its degradation and reduction in fluorescence intensity. The DPBF loss was measured through the reduction in its fluorescence intensity at 490 nm, upon excitement at 405 nm. An FA-PEG@BPQD@DOX of 20 μl (30 μg/ml of P, determined by inductively coupled plasma mass spectrometry) was added with 2 ml of DPBF (12 mM), followed by irradiation for equal intervals. The reduction in DPBF absorbance intensity indicates the ROS production during the BPQD photosensitization. The rate of DPBF degradation with irradiation time was used for measuring the ROS yields due to the proportional relationship.

2.7 Photothermal heating experiment

Typically, the NIR photothermal effect was measured by employing a consecutive 808-nm NIR laser. A quartz cuvette with a 1-cm path length, containing 0.5 ml of FA-PEG@BPQD@DOX, was exposed to a laser of 1.0 W/cm^2, covering the whole sample surface. A thermocouple microprobe ($\varphi = 0.5$ mm) was submerged in the solution for monitoring the temperature. Using an infrared camera, the *in vivo* real-time thermal images were obtained for the measurement of the highest temperature.

2.8 Cell culture

Human embryonic kidney 293T (HEK 293T) cells were purchased from Shanghai Meixuan Biotechnology Co., Ltd. (China). These cells were cultured in DMEM containing 10% calf serum, 100 U/ml of penicillin, 100 mg/ml of streptomycin, and 100 mg/ml of neomycin at 37°C with 5% CO_2.

2.9 *In vitro* cytotoxicity assay

The cytotoxicity of FA-PEG@BPQD@DOX was evaluated in 293T cells using MTT assays. Briefly, 293T cells in the

logarithmic growth phase were transferred to a 96-well plate for 24 h, and FA-PEG@BPQD@DOX (0, 50, 100, 150, 200, and 250 μg/ml) was added for another 24 h. Cells cultured in the medium alone served as the control. Then, the medium was removed, and 10 μl of MTT (5 mg/ml) was added for 1.5 h. The optical density at 450 nm was read using an iEMSAnalyzer (Lab-system) and compared to that of the control cells (n = 4 wells per group).

2.10 Synergistic antitumor efficacy of *in vitro* PDT/PTT/chemotherapy

In order to determine the antitumor efficacy of FA-PEG@BPQD@DOX, 293T cells were transferred into a 96-well plate at a density of 1×10^5 cells/well and incubated overnight. Then, FA-PEG@BPQD@DOX of different concentrations was added overnight. Afterward, these cells were washed twice before being illuminated at 808 nm (1 W/cm^2). The 293T cells were further cultured for 24 h, and the viability was assessed using the MTT method.

2.11 Animal model

All animals were manipulated in accordance to the rules issued by the Institutional Committee for Animal Care and the National Ministry of Health. HeLa cells were subcutaneously seeded into 4-week-old BALB/c female nude mice (Shanghai BK Laboratory Animal, China).

2.12 *In vitro* and *in vivo* PA imaging

All images were obtained using an optoacoustic tomographic imaging system (VevoLAZR; FujiFilm VisualSonics, Mountain View, CA, USA) for both the *in vitro* phantom and *in vivo* experiments, with a consecutive excitation at 680–970 nm and a 2-cm focal depth. The *in vitro* absorption wavelength of FA-PEG@BPQD@DOX was measured between 680 and 970 nm and was at the maximum at 680 nm. A laser of 680 nm was used to acquire the signals of the PA and US.

For the *in vivo* PA imaging, 3×10^6 293T cells (100 μl) were subcutaneously injected into the right foreleg of mice. Then, these tumors were allowed to grow to 150 mm^3 within 2 weeks. The FA-PEG@BPQD@DOX or PEG@BPQD@DOX solution was administered via the tail vein. The PA images were taken at 0, 2, 4, 6, and 24 h postinjection. During the scans, these animals were anesthetized with 1%–2% isoflurane, with the body temperature maintained at 37.5°C.

2.13 Synergistic antitumor efficacy of *in vivo* PDT/PTT/chemotherapy

A total of 2×10^7 293T cells were subcutaneously injected into the flank of mice. Then, the tumor was allowed to grow to 100 mm^3. Afterward, these animals were arbitrarily divided into four groups, with six mice per group: tail vein injected with PBS as control group (G1); tail vein injected with PEG@BPQD@DOX with laser irradiation (G2); tail vein injected with FA-PEG@BPQD@DOX (G3); and tail vein injected with FA-PEG@BPQD@DOX with laser irradiation (G4). Nanomaterials of the same amount of P were injected into the tumors in mice in G2–G4. At 4 h after injection, the lung tumor sites were irradiated (808 nm, 2 W/cm^2, 20 min). The tumor growth and body weight were monitored to evaluate the treatment effect of the PDT/PTT/chemotherapy. The volume of tumors (V) was calculated using the following formula:

$$V = \frac{\text{tumor length} \times \text{tumor width}}{2}$$

2.14 Histological examination

One mouse in each group was euthanized after the antitumor therapy. The lung, heart, kidney, liver, and spleen were resected. The tissues were stained with hematoxylin and eosin (H&E). Briefly, a small tissue block was fixed with 10% formalin, paraffin-embedded, cut into 8-μm sections, and stained. These sections were imaged using a microscope (Leica QWin, Leica TCS SP8 CARS, Leitz, Wetzlar, Germany).

3 Results and discussion

The morphology of BPQDs was examined using TEM; the presence of ultrasmall BPQDs was confirmed (Figure 2A). Lattice fringes with an interplanar spacing of 0.34 nm were presented in the high-resolution TEM (HRTEM) images, which was very similar to the (021) planes of the BP (Figure 2B, C). The single-crystal nature of the BP NPs is shown in the fast Fourier transform image (Figure 2D). The topographic morphology of BPQDs was presented by AFM (Figure 2E), and the thickness was measured using cross-sectional analysis. The height measurements of 1.19, 0.63, 1.23, 0.60, and 0.61 nm corresponded to BPQDs with approximately 1 or 2 layers, respectively. The mean lateral size of 200 BPQDs revealed by TEM was 5.5 ± 2.0 nm (Figure 2F). The X-ray diffraction revealed that BPQDs have a similar crystal structure to that of the

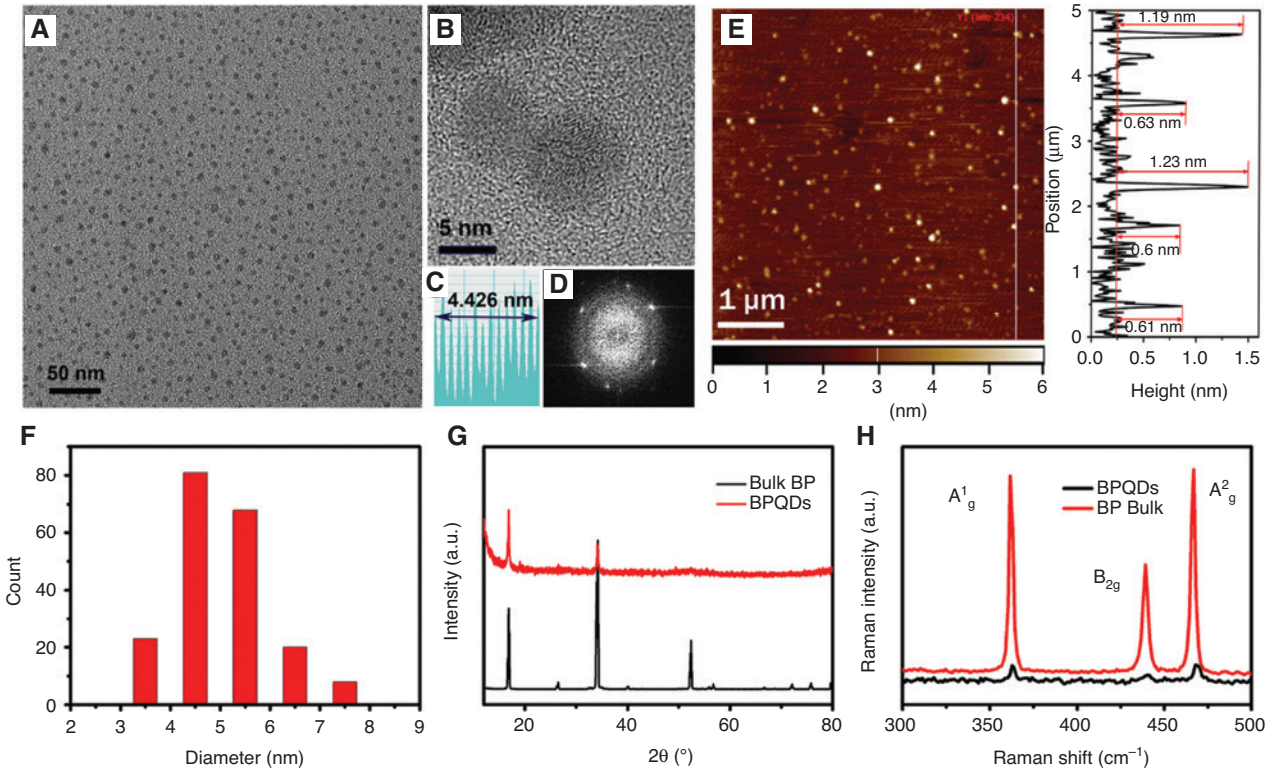

Figure 2: Morphology and characterization.
(A) The examination of BPQDs, the HRTEM images of lattice fringes (B and C), and the fast Fourier transform (D) using TEM. (E) The AFM imaging (left). The white line denotes the height profiles (right). (F) The histogram of the sizes of 200 BPQDs measured from the TEM image. (G) The X-ray diffraction pattern of bulk BP and BPQDs. (H) The Raman spectra of BPQDs and the bulk BP.

bulk BP (Figure 2G). Three typical Raman peaks of BP corresponded to the out-of-plane vibration mode A_g^1 and the in-plane vibration modes B_{2g} and A_g^2, respectively (Figure 2H). It can be observed that the three Raman peaks of BPQDs all variously red-shifted from the bulk BP, suggesting that the mean thickness of the BPQDs was pretty small [26].

The characterizations of various concentrations of BPQDs were performed using UV-vis-NIR absorption spectroscopy (Figure 3A). The FA-adorned pegylated BPQD was produced by coating the FA-PEG conjugate (FA-PEG-NH_2) on the surface of BPQDs. After FA-PEG-NH_2 coating, the FA-PEG@BPQD NPs had a peak of UV/Vis absorbance at 280 nm, showing the existence of FA in the NPs (Figure 3B). The optical absorption spectra of the FA-PEG@BPQD exhibited a wide band that covered UV-vis-NIR spectra stronger than BPQDs, owing to the FA-PEG. Moreover, as previously reported, BPQDs functionalized with FA-PEG-NH_2 also can improve their biocompatibility and physiological stability [27–29].

Many 2D nanomaterials, such as graphene and TMDs, have been used as drug carriers due to their high surface area [30]. Black phosphorus quantum dot–based materials are expected to have high loading abilities. The calculation of the drug loading capacity was performed based on DOX concentrations in the supernatant. Higher DOX concentrations (0–3.5 μg/ml) resulted to a higher loading capacity of DOX, showing a linear relationship and a saturation level at 2.5 (Figure 3C). The saturation of DOX loading was approximately 65% in the present study, which was significantly higher than the 10%–30% of the drug loading capacity of a previously reported NPbased nanodelivery.

The DLS revealed that the mean size of the PEG-FA–modified BPQD (8 ± 1 nm) was slightly greater than the BPQD (6.5 ± 1 nm) (Figure 3D, E). In order to investigate the ROS generation of these BPQDs, DPBF was used as an ROS indicator, with PBS as the control. These BPQDs dramatically decreased the DPBF absorbance at 410 nm with 808-nm excitement (1 W/cm^2), while the FA-PEG@BPQD@DOX resulted in almost the same decrease in the DPBF absorbance with the same laser irradiation conditions (Figure 3F). These results suggest that the modification has no effect on the ROS production of BPQDs. In order to determine whether the reaction was induced by the produced $^1O_2$, sodium azide (NaN_3) was added with ultrathin

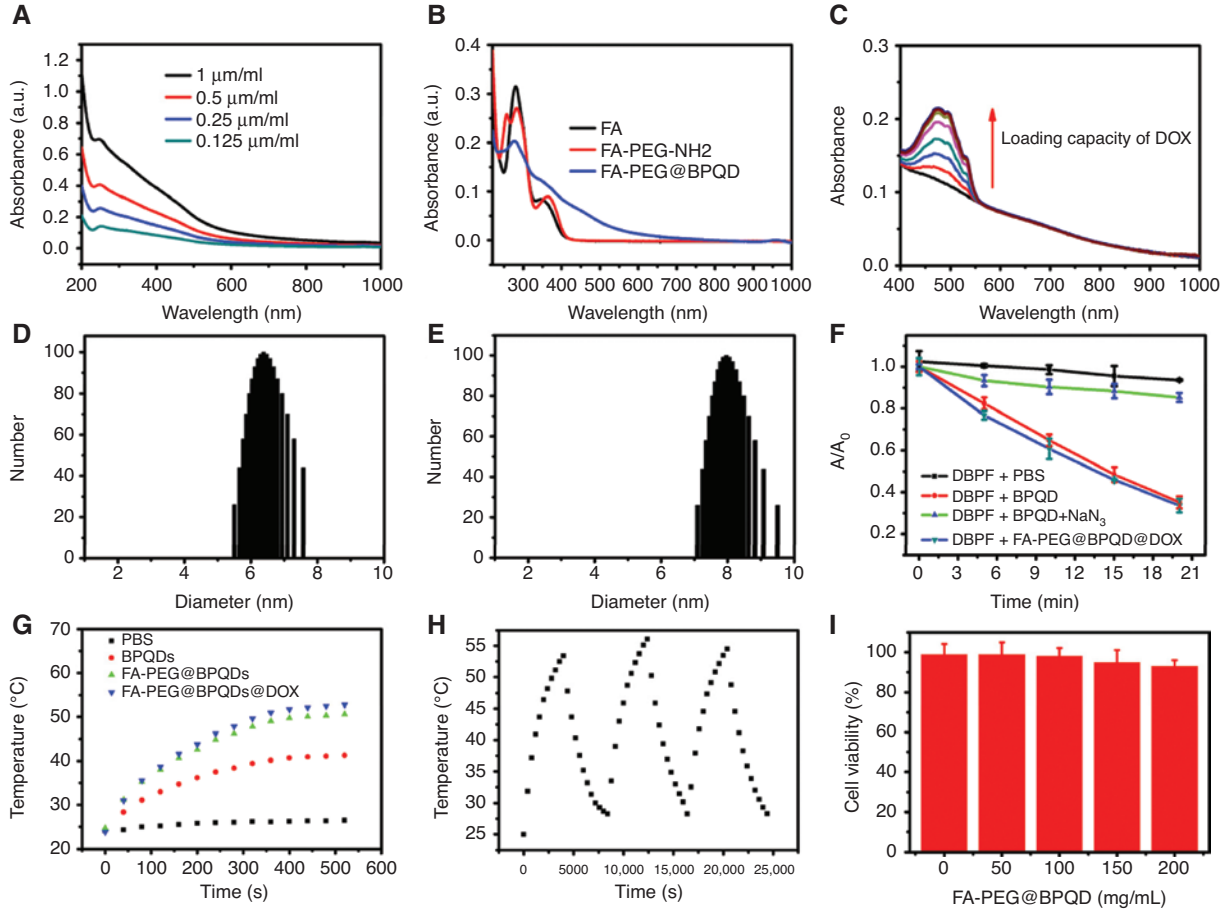

Figure 3: Characterization of FA-PEG@BPQD@DOX.
(A) The ultraviolet-vis-NIR spectra of BPQDs of different concentrations in water. (B) The absorbance spectra of FA, FA-PEG-NH_2 and FA-PEG@BPQD. (C) The DOX loading capacities of FA-PEG@BPQD with different DOX concentrations. (D and E) The particle size distribution of BPQD before and after this was FA-PEG coated and measured by DLS. (F) The normalized absorbance of DPBF when BPQDs were present. (G) The photothermal heating curves of BPQDs in different conditions (1 ml, BPQD = 100 μg/ml) under laser irradiation (2 W/cm^2, 808 nm). (H) The photothermal heating/cooling curves of FA-PEG@BPQD@DOX (1 ml, BPQD = 100 μg/ml) with laser on/off. (I) The viability of 293T cells in various concentrations of FA-PEG@BPQD.

BPQD to consume $^1O_2$. After the addition of NaN_3, no significant change in the absorption of DPBF was noticed, even after the laser irradiation for 15 min, suggesting that $^1O_2$ was the active species generated by BPQD (Figure 3F).

The temperature of the FA-PEG@BPQD dispersion significantly increased, when compared to PBS, if both were treated with laser irradiation (1 W/cm^2, 808 nm; Figure 3G). The photothermal performance FA-PEG@BPQD@DOX was almost the same as FA-PEG@BPQD but was superior to that of BPQDs. This could be explained by the better optical absorbance after coating with FA-PEG. The temperature of the FA-PEG@BPQD@DOX dispersions raised to the highest depicted negligible difference, even with three cycles of laser on/off (Figure 3H), suggesting the good photothermal stability with laser treatment.

The biocompatibility of FA-PEG@BPQD was investigated (Figure 3I). The 293T cells were incubated with FA-PEG@BPQD at 200 μg/ml for 24 h, and no obvious cytotoxicity was found (200 μg/ml).

All these results suggest that FA-PEG@BPQD@DOX has low cytotoxicity, excellent PDT and PTT effect, and high drug loading capacity.

The internalization of the drug nanostructure system into 293T cells was investigated by tracking the DOX signal (red fluorescence) (Figure 4). The incubation with FA-PEG@BPQD@DOX for 2 h significantly increased the DOX fluorescence intensity, when compared to PEG@BPQD@DOX. This result suggests that FA conjugation increased the binding and uptake of NPs to FR-positive 293T cells. The fluorescence of both FA-PEG@BPQD@DOX and PEG@BPQD@DOX was initially observed in the cytoplasm and was observed in the nuclei after laser irradiation, indicating that DOX-loaded BPQDs are internalized through the endocytosis pathway and localized in cellular compartments, and finally, the

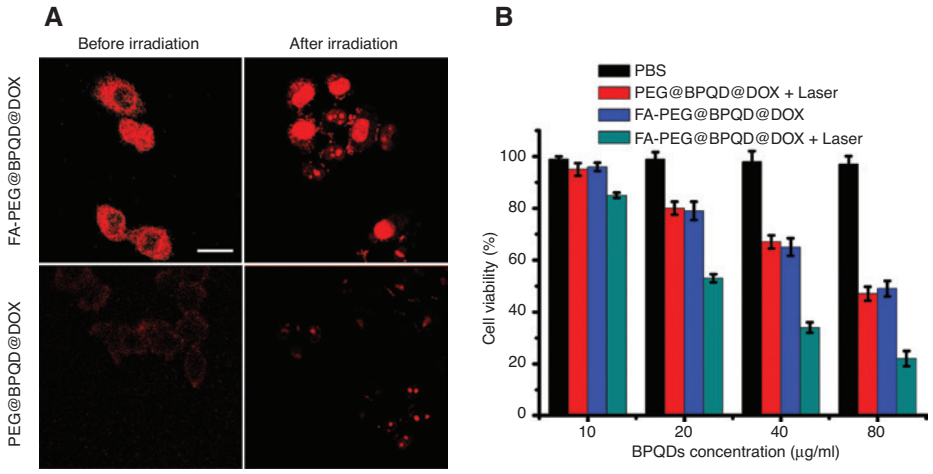

Figure 4: *In vitro* imaging and anticancer effect of FA-PEG@BPQD@DOX drug delivery platform.
The confocal microscopy of 293T cells treated with (A) FA-PEG@BPQD@DOX and PEG@BPQD@DOX. The bar in A is 20 μm. (B) The cell viability after incubation with BPQDs-based NPs with 808-nm laser irradiation (1 W/cm², 15 min).

loaded DOX is released into the nuclei (Figure 4A). These results show that FA-PEG@BPQD@DOX can release these drugs in response to the NIR laser.

The synergistic effects of the PDT, PTT, and chemotherapy of this BPQDs-based nanosystem were evaluated *in vitro*. The highest cytotoxicity was found in the FA-PEG@BPQD@DOX + laser group due to the synergistic effect (Figure 4B). The FA-PEG@BPQD@DOX + laser group had a higher cytotoxicity, when compared to the PEG@BPQD@DOX + laser group. These results could be explained by the slower endocytosis of PEG@BPQD@DOX and its nontargeting nature.

Mice with 293T tumors were treated with or without the targeted BPQDs-based drug delivery system, and the thermal images were taken. No significant change in temperature was noticed in the control group, even after 300 s of irradiation at 808 nm (2 W/cm², Figure 5A). In the PEG@BPQD@DOX group, 5 min of NIR irradiation mildly increased the tumor site temperature to 44.2°C, because the nontargeting NPs coated with PEG did not effectively target the tumor sites. However, after 4 h and the intravenous injection of FA-PEG@BPQD@DOX, the tumor site temperature rapidly increased along with the irradiation duration. The irradiation of 300 s at 808 nm (2 W/cm²) rapidly raised the temperature to 56.8°C, which is sufficient for killing tumor cells. These present findings show that FA-PEG@BPQD@DOX has a good PTT effect and accurate targeting ability for tumor ablation.

The as-fabricated FA-PEG@BPQD@DOX composites were examined for the PA properties. The light in the "NIR optical window" has deeper tissue penetration and reduced photodamage and was usually considered a promising method for *in vivo* imaging. FA-PEG@BPQD@DOX was tested with various NIR wavelengths to examine its performance. The increase in the laser wavelength from 680 to 980 nm decreased the PA signal intensity (Figure 6).

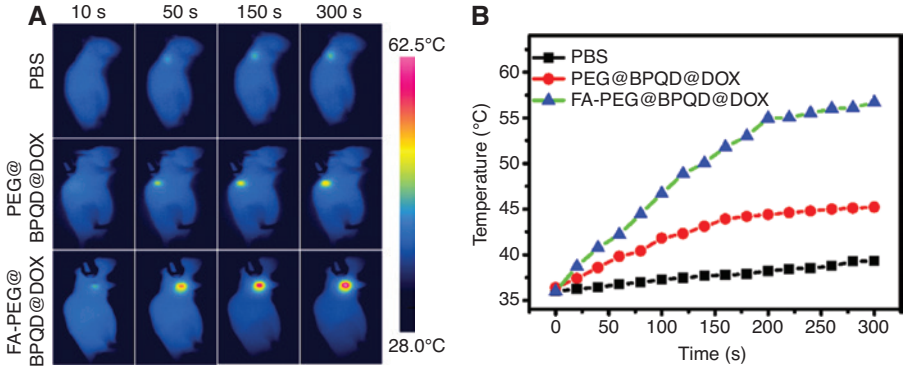

Figure 5: *In vivo* photothermal effects of FA-PEG@BPQD@DOX.
(A) The thermal images of mice with 293T tumors irradiated at 808 nm (2 W/cm²). These mice were injected with PBS, PEG@BPQD@DOX, or FA- PEG@BPQD@DOX. (B) The temperature of mice irradiated at 808 nm (2 W/cm²).

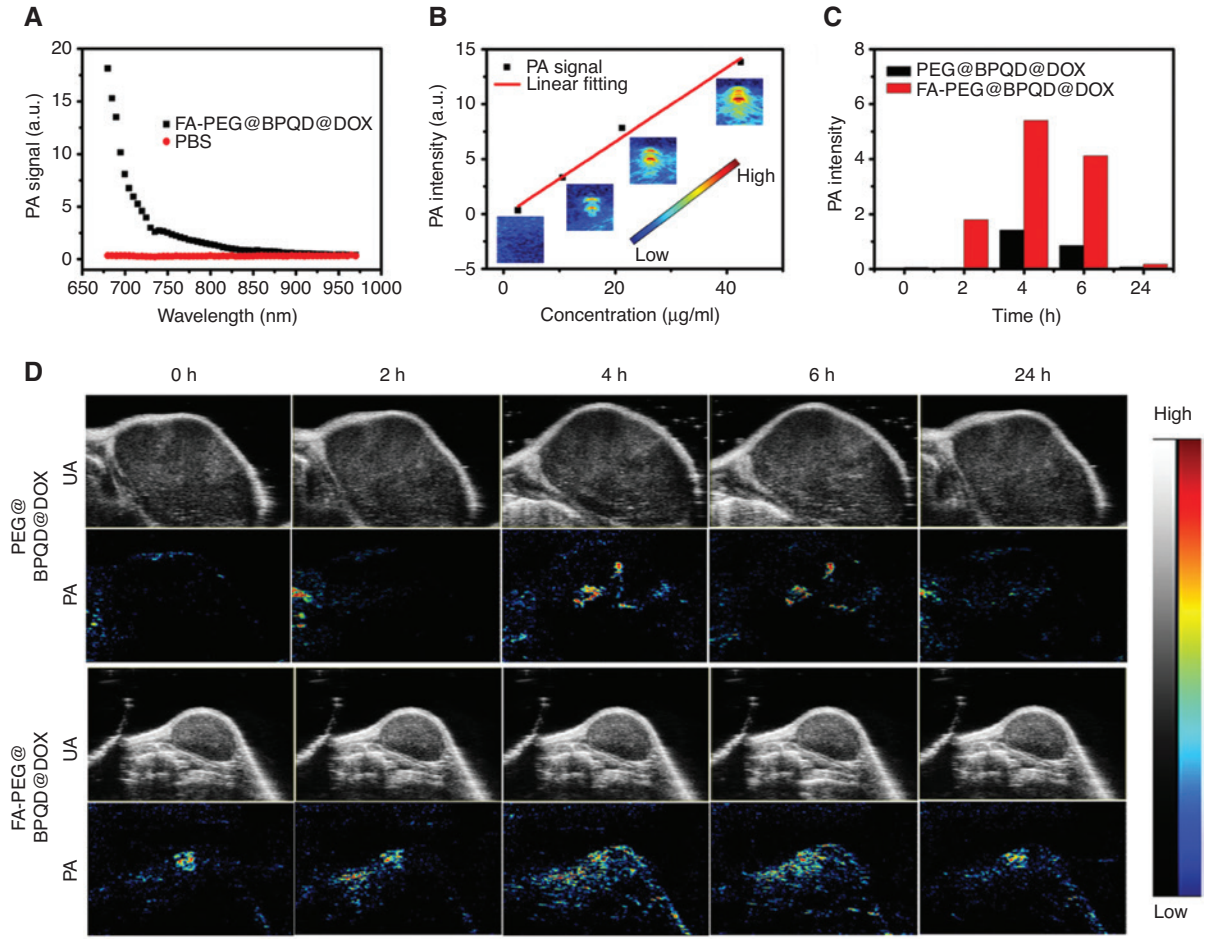

Figure 6: PA performance of FA-PEG@BPQD@DOX.
(A) The PA spectrum of FA-PEG@BPQD@DOX and PBS. (B) The FA-PEG@BPQD@DOX NP dispersions of different concentrations were irradiated at 680 nm to obtain the PA images and the corresponding PA signal intensity. (C) The quantified PA signals in tumors. (D) The tumor PA images after injecting PEG@BPQD@DOX and FA-PEG@BPQD@DOX NPs with irradiation at 680 nm.

A laser irradiation shorter than the thermal transport time of the absorbed energy can cause transient thermoelastic expansion and a subsequent PA pressure wave in optical absorbing materials, such as BPQDs. The efficiency of converting light energy to PA pressure wave is critical for generating the PA signals during the thermal expansion in an optical absorber. The conversion efficiency is primarily determined by the light absorbance and heat capacity of the optical absorber. Therefore, the PA signal intensity of the FA-PEG@BPQD@DOX diminished when the optical absorption decreased from 680 to 980 nm. These results suggest that 680 nm produced the optimal signal and was used for the subsequent tests. The FA-PEG@BPQD@DOX of various concentrations from 0.3 to 50 μg/ml was irradiated at 680 nm, and the PA images and corresponding PA signal intensities were examined (Figure 6B). As the nanoparticle concentration was increased from 0.3 to 50.0 μg/ml, the enhancement of the PA signal exhibited a linear relationship with the concentration of BPQDs. These findings suggest that FA-PEG@BPQD@DOX has good potential for *in vivo* PA imaging and PTT. FA-PEG@BPQD@DOX NPs were injected into tumor-bearing mice, and tumor PA images were taken (Figure 6D). Weak signals in the tumors were shown by the precontrast images. After the BP NPs were intravenously injected, the contrasts of the tumor were significantly increased along with longer circulation time, suggesting the accumulation of BP NPs in the tumor.

The antitumor efficacy of FA-PEG@BPQD@DOX when utilizing the combination of PDT, PTT, and chemotherapy was investigated *in vivo*. Mice with 239T tumors were randomly assigned into four groups (n = 6 per group): (G1) PBS alone, (G2) PEG@BPQD@DOX plus 808-nm laser, (G3) FA-PEG@BPQD@DOX only, and (G4) FA-PEG@BPQD@DOX plus 808-nm laser. Phosphate-buffered saline (100 μl) or PEG@BPQD@DOX, FA-PEG@

BPQD@DOX (200 μg/ml) was administrated via intravenous injection. After conducting different treatments, the body weight and tumor volumes were measured every 4 days. The treatment with FA-PEG@BPQD@DOX and 808-nm irradiation significantly inhibited the tumor growth, and the triple therapy achieved the smallest tumor (Figure 7A). All groups exhibited no significant body weight loss, suggesting the generally good safety of NPs and laser irradiation (Figure 7B). Mice in G1, G2, and G3 exhibited a significant increase in tumor volumes. However, mice in G4 exhibited a significant inhibition in tumor growth (Figure 7C). These results could be explained by the nontargeting nature of PEG@BPQD@DOX nanocomposites and its low concentration in tumors.

Remarkably, in G4, 100% of mice survive through the 40-day study period (Figure 7D). In comparison, the treatment with PBS, PEG@BPQD@DOX and laser irradiation, and FA-PEG@BPQD@DOX alone showed significantly shorter survival times. The tumors obtained from mice treated with FA-PEG@BPQD@DOX and 808-nm laser were smaller than those obtained from mice that received other treatments (Figure 7E). The H&E staining of the major organs revealed no obvious inflammation in the other three treatment groups, when compared with the control group, suggesting the good safety of the present NPs (Figure 7F).

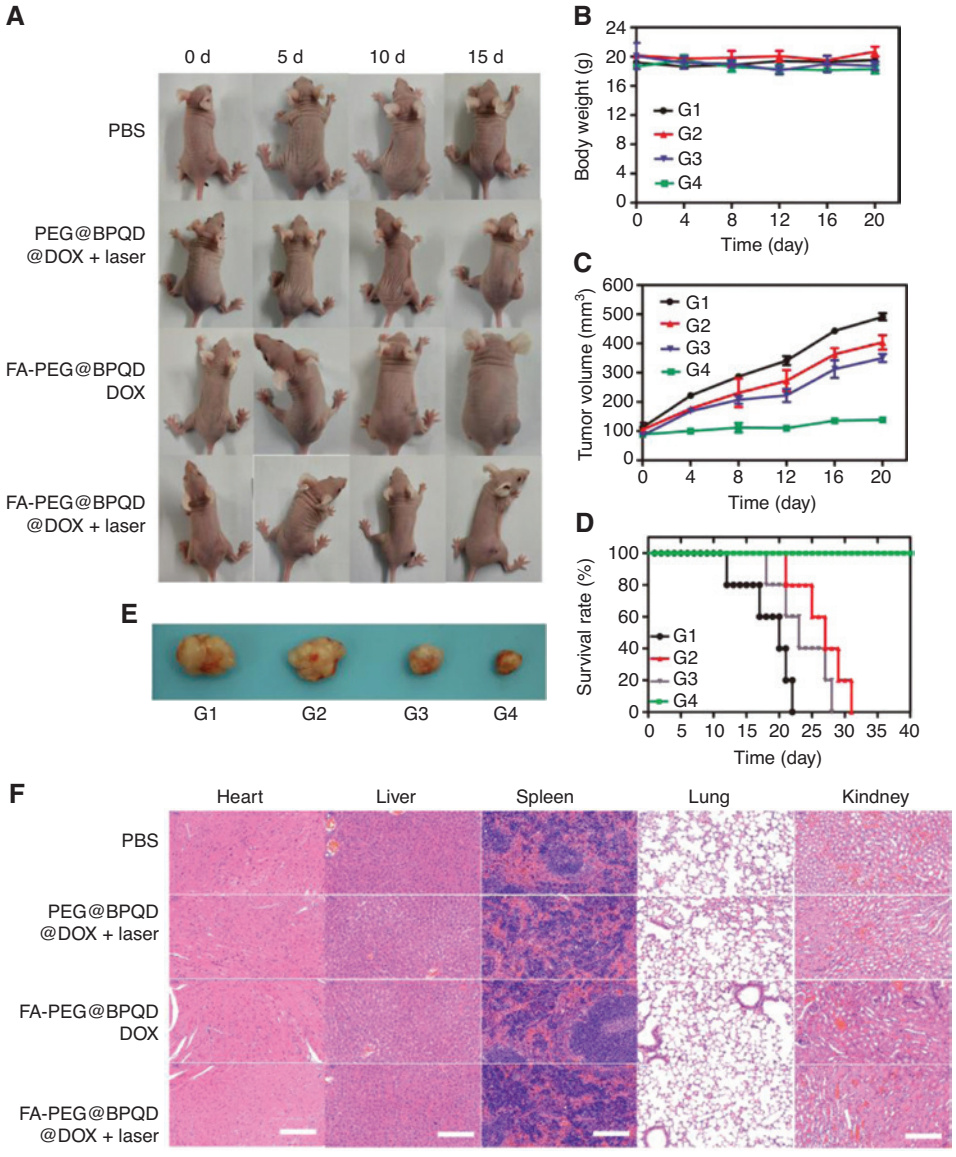

Figure 7: *In vivo* therapeutic effects of FA-PEG@BPQD@DOX.
(A) The images of mice injected with different agents. (B) The changes in body weight and (C) tumor volume of the mice. (D) The survival analysis of mice. (E) The resected tumors after PDT treatment for 20 days. (F) The H&E staining results.

4 Conclusion

A BPQDs-based nanoplatform with drug delivery capability and triple collaborative targeted tumor therapy was designed. The BPQD exhibited a significantly higher loading capacity for DOX. FA-PEG@BPQD@DOX NPs had good biocompatibility and can be efficiently internalized by targeted cells. The nanosheet-like nanocarriers release the drug in prompt response to the NIR laser irradiation. Black phosphorus quantum dots can be used as both PDT and PTT agents. The BP-based drug delivery system with targeted synergistic PDT, PTT, and chemotherapy exhibited an excellent antitumor effect in mice. These results present the potential of FA-PEG@BPQD@DOX NPs as a promising cancer therapy with good biological safety.

Acknowledgments: This work was supported by grants from the National Natural Science Foundation of China (61527821, 61521093, and 11804350), the Instrument Developing Project (YZ201538), the Strategic Priority Research Program of the Chinese Academy of Sciences (XDB160106), the Shanghai Municipal Science and Technology Major Project (2017SHZDZX02), and the Shanghai Sailing Program (17YF1421300).

Declaration of interest: None.

References

[1] Bray F, Jemal A, Grey N, et al. Global cancer transitions according to the Human Development Index (2008–2030): a population-based study. Lancet Oncol 2012;13:790–801.
[2] Bray F, Ferlay J, Soerjomataram I, et al. Global cancer statistics 2018: GLOBOCAN estimates of incidence and mortality worldwide for 36 cancers in 185 countries. CA Cancer J Clin 2018;68:394–424.
[3] Allen C, Her S, Jaffray DA. Radiotherapy for cancer: present and future. Adv Drug Deliv Rev 2017;109:1–2.
[4] Zhou R, Wang H, Yang Y, et al. Tumor microenvironment-manipulated radiocatalytic sensitizer based on bismuth heteropolytungstate for radiotherapy enhancement. Biomaterials 2019;189:11–22.
[5] Cheng K, Yang X, Zhang X, et al. High security nanocluster for switching photodynamic combining photothermal and acid-induced drug compliance therapy guided by multimodal active-targeting imaging. Adv Funct Mater 2018;28:1803118.
[6] Meng X, Liu Z, Cao Y, et al. Fabricating aptamer-conjugated PEGylated-MoS2/$Cu_{1.8}$S theranostic nanoplatform for theranostic nanoplatform for multiplexed imaging diagnosis and chemo-photothermal therapy of cancer. Adv Funct Mater 2017;27:1605592.
[7] Lv R, Yang P, He F, et al. An imaging-guided platform for synergistic photodynamic/photothermal/chemo-therapy with pH/temperature-responsive drug release. Biomaterials 2015;63:115–27.
[8] Vankayala R, Hwang KC. Near-infrared-light–activatable nanomaterial-mediated phototheranostic nanomedicines: an emerging paradigm for cancer treatment. Adv Mater 2018;30:1706320.
[9] Choi JR, Yong KW, Choi JY. Black phosphorus and its biomedical applications. Theranostics 2018;8:1005–26.
[10] Fan T, Zhou Y, Qiu M, et al. Black phosphorus: a novel nanoplatform with potential in the field of bio-photonic nanomedicine. J Innovative Opt Health Sci 2018;11:1830003.
[11] Luo M, Fan T, Zhou Y, Zhang H, Mei L. 2D black phosphorus–based biomedical applications. Adv Funct Mater 2019;29:1808306.
[12] Lee HU, Park SY, Lee SC, et al. Black phosphorus (BP) nanodots for potential biomedical applications. Small 2016;12:214–9.
[13] Tao W, Kong N, Ji XY, et al. Emerging two-dimensional monoelemental materials (Xenes) for biomedical applications. Chem Soc Rev 2019;48:2891.
[14] Zhang Y, Lim C, Dai Z, et al. Photonics and optoelectronics using nano-structured hybrid perovskite media and their optical cavities. Phys Rep 2019;795:1–51.
[15] Fan T, Xie Z, Huang W, Li Z, Zhang H. Two-dimensional non-layered selenium nanoflakes: facile fabrications and applications for self-powered photo-detector. Nanotechnology 2019;30:114002.
[16] Wang H, Yang X, Shao W, et al. Ultrathin black phosphorus nanosheets for efficient singlet oxygen generation. J Am Chem Soc 2015;137:11376–82.
[17] Sun Z, Xie H, Tang H, et al. Ultrasmall black phosphorus quantum dots: synthesis and use as photothermal agents. Angew Chem Int Ed Engl 2015;54:11526–30.
[18] Pravst I. Risking public health by approving some health claims? The case of phosphorus. Food Policy 2011;36:726–8.
[19] Wang W, Cheng D, Gong F, et al. Design of multifunctional micelle for tumor-targeted intracellular drug release and fluorescent imaging. Adv Mater 2012;24:115–20.
[20] Rosenholm JM, Meinander A, Peuhu E, et al. Targeting of porous hybrid silica nanoparticles to cancer cells. ACS Nano 2009;3:197–206.
[21] Feng D, Song Y, Shi W, et al. Distinguishing folate-receptor–positive cells from folate-receptor–negative cells using a fluorescence off-on nanoprobe. Anal Chem 2013;85:6530–5.
[22] Liang B, He ML, Xiao ZP, et al. Synthesis and characterization of folate-PEG–grafted-hyperbranched-PEI for tumor-targeted gene delivery. Biochem Biophys Res Commun 2008;367:874–80.
[23] Low PS. Folate receptor–targeted drugs for cancer and inflammatory diseases. Adv Drug Deliv Rev 2004;56:1055–8.
[24] Guo T, Wu Y, Lin Y, et al. Black phosphorus quantum dots with renal clearance property for efficient photodynamic therapy. Small 2017;14:1702815.
[25] de Sousa M, Visani de Luna LA, Fonseca LC, Giorgio S, Alves OL. Folic-acid functionalized graphene oxide nanocarrier: synthesis, approaches, characterization, drug delivery study, and antitumor screening. ACS Appl Nano Mater 2018;1:922–32.
[26] Guo Z, Zhang H, Lu S, et al. From black phosphorus to phosphorene: basic solvent exfoliation, evolution of Raman scattering, and applications to ultrafast photonics. Adv Funct Mater 2015;25:6996–7002.

[27] Guo Z, Chen S, Wang Z, et al. Metal-ion–modified black phosphorus with enhanced stability and transistor performance. Adv Mater 2017;29:1703811.
[28] Tang X, Liang W, Zhao J, et al. Fluorinated phosphorene: electrochemical synthesis, atomistic fluorination, and enhanced stability. Small 2017;13:1702739.
[29] Sang DK, Wang H, Guo Z, et al. Recent developments in stability and passivation techniques of phosphorene toward next-generation device applications. Adv Funct Mater 2019:1903419.
[30] Chen H, Liu T, Su Z, et al. 2D transition metal dichalcogenide nanosheets for photo/thermo-based tumor imaging and therapy. Nanoscale Horiz 2018;3:74–89.